Dongil Shin
Department of Mechanical Engineering,
Texas A&M University,
College Station, TX 77840
e-mail: davshin@tamu.edu

Junho Suh
Professor
School of Mechanical Engineering,
Pusan National University,
2 Busandaehak-ro 63beon-gil, Geumjeong-gu,
Busan 46241, South Korea
e-mail: junhosuh@pusan.ac.kr

Alan B. Palazzolo
Professor
Department of Mechanical Engineering,
Texas A&M University,
College Station, TX 77840
e-mail: a-palazzolo@tamu.edu

Parametric Study of Flexure Pivot Bearing Induced Thermal Bow-Rotor Instability (Morton Effect)

This paper investigates the journal asymmetric temperature-induced thermal bow vibration of a rotor, as supported by a flexure pivot journal bearing (FPJB). Thermal bow-induced vibration, known as the Morton effect (ME), is caused by non-uniform viscous heating of the journal, and the resulting thermal bow often causes increasing vibration amplitudes with the time-varying phase. Full FPJB's structural and thermal finite element models are developed and integrated into the flexible rotor model. The model is validated by comparing its predicted ME response with experimental results. An FPJB model, which uses predicted "equivalent" radial and tilting stiffness of the bearing, is compared with the full finite element method (FEM)-based model. The impact of FPJB's design parameters such as web thickness, bearing material, and housing thicknesses are investigated with parametric studies. The results show that FPJB parameter values may have a major effect on the speed range of ME vibration, and its severity. [DOI: 10.1115/1.4052679]

Keywords: *bearings, fluid film lubrication, journal bearings*

1 Introduction

The Morton effect (ME) is caused by non-uniform heating around the journal circumference inducing a peak differential temperature (ΔT) across the journal, at the hot spot location. The differential causes a thermal bow of the shaft, which further dynamically excites the system at the synchronous frequency. If the rotor orbit, journal ΔT, and thermal bow form a loop with positive feedback gain, the spiral vibration which may form diverging, non-converging, or converging motions will appear accompanied with unusually high journal ΔT. Reported occurrences of the ME, as identified by slowly varying synchronous vibration amplitude and phase angle, have steadily increased since the 1990s [1–5]. With the growing interest and cases in the ME, many experimental and numerical studies have been studied.

Pioneering works of ME experiments were reported before the 2000s in Refs. [6–13]. Morton [6] first reported the existence of journal ΔT in a journal circumference by measuring the journal temperature values at 1800 rpm. de Jongh and Morton [7] employed a rotor supported by tilting pad journal bearing (TPJB) to investigate the ME. Four temperature sensors were used to measure the journal ΔT and detected the maximum ΔT of 10 °C along with spiraling vibrations at 11,200 rpm. They showed that the ME instability could be avoided by quickly raising the rotor operating speed. de Jongh and Van Der Hoeven [8] presented a single overhung rotor experiencing the ME around 8000 rpm. The authors alleviated the ME vibration by applying a heat sleeve between the journal and bearing, which reduces heat input to the journal. Berot and Dourlens [9] investigated the ME instability in a single overhung rotor, and large spiral vibration was observed near 6510 rpm where changes in oil supply temperature and rotor speed induced the instability.

To better understand the ME, many mathematical models including simplified models and finite element method (FEM)-based high-fidelity model have been developed, and its simulation results were verified with the experimental results. Keogh and Morton [10] employed a simple numerical model to investigate the journal asymmetric heating. The model assumed steady-state, synchronous journal orbiting in their rotor dynamic model, along with a time-varying shaft bending effect. The same authors [11] conducted a stability analysis of a rotor by incorporating the thermal bending effect. A computational fluid dynamics (CFD) technique was first applied by Tucker and Keogh [12] to investigate the dynamic and thermal states of a journal-bearing subject to whirling motion. They discovered that significant ΔTs can be developed on the journal circumference with large journal orbits. Gomiciaga and Keogh [13] analyzed a non-centered orbit case and calculated the heat input into the journal. The authors showed that the heat input into the journal varies sinusoidally. The Kellenberger method [14] which was originally developed to predict the rotor-stator rub by estimating the heat input to the shaft was also widely used for predicting the ME. Kirk et al. [15] employed the simplified one-dimensional (1D) energy equation was used to predict the film temperature of journal bearing and suggested an unbalance threshold method that considers the resultant value calculated from both mechanical and thermal unbalances. Other simplified ME prediction methods determining the ME instability employing hot spot stability and linear relations were developed in Refs. [16,17]. Childs and Saha [18] employed forward and backward whirls to estimate the journal thermal gradient and predicted the ME instability onset speed.

Finite element method is adopted to accurately predict the fluid film force of journal bearing and thermal/mechanical deformations of the bearing/rotor structures of the rotor in the 2010s. Palazzolo and his co-authors [19–24] developed high-fidelity prediction algorithms for the ME employing finite element methods and nonlinear transient simulation. The energy equation for fluid film temperature and thermal/structural models for bearing and shaft were developed and used for the ME prediction. Tong and Palazzolo [25] have shown that the ME instability may occur in the rotor supported by gas-lubricated bearing from their numerical simulations. Panara et al. [26] suggested an iterative FEM thermo-structural approach for ME analysis and verified its accuracy with experimental results. Shin and Palazzolo [27,28] numerically investigated journal misalignment and pad pivot effects on the ME instability, and the same authors [29] showed that installing a squeeze film damper may mitigate ME instability. While most ME research focused on the overhung rotor type, Guo and Kirk [30,31] numerically proved that the ME instability could occur in a midspan rotor as well as an overhung rotor.

Recently, more case histories and experimental investigations for the ME have been reported [32–35]. Lorenz and Murphy [32] analyzed the ME instability case of the rotor running at

Contributed by the Tribology Division of ASME for publication in the Journal of Tribology. Manuscript received June 2, 2021; final manuscript received October 3, 2021; published online December 22, 2021. Assoc. Editor: Patrick S. Keogh.

4200 rpm. The instability was suppressed by replacing the partial arc bearing with the four-lobed fixed bearing. Tong and Palazzolo [33] measured the journal temperature differential employing 20 temperature sensors installed at a journal circumference. The authors compared the measured temperatures with the ME prediction models including the simplified and high-fidelity ME prediction models. The results showed that the high-fidelity model presents better agreement with the measured temperatures compared to the simplified version. Hresko et al. [34] built a Morton experimental rig equipped with a single overhung mass and TPJB. A total number of 26 temperature sensors were equipped to measure the journal temperature differential. Plantegenet et al. [35] conducted the ME experiment with a rotor supported by a plain journal bearing. The instability leading to the journal-bearing rub was observed with the long bearing at 6600 rpm speed.

Although many numerical and experimental works on ME have been conducted, most of the works focused on the rotor supported by TPJBs. The ME studies on many other types of bearings, such as flexure pivot FPJB, pressure dam bearing, floating ring bearing, etc., have not been actively conducted compared to the studies on the TPJBs. The only reported works on the FPJB-ME effect were presented in Refs. [36,37], which demonstrated the ME instability in the FPJB by observing clear spiral vibration at both 6550 rpm and 6850 rpm speeds. The flexible pivot design of the FPJB has many favorable features compared to the conventional tilting pivot which rocks or slides on housing surfaces. For example, the flexure pivot prevents pivot wear which helps maintain certain bearing performance features, such as preload. To explain the favorable features of the FPJB due to its pivot design, many experimental works were conducted. Walton and San Andres [38] measured the static performances of a four-pad FPJB for operating speeds from 1800 to 4500 rpm. A numerical model was employed to verify the experimental measurements. Rodriguez and Childs [39] and Al-Ghasem and Childs [40] measured the dynamic stiffness of the FPJB for load-on-pad and load-between-pad configurations, respectively. Hensley and Childs [41] expanded the work in Ref. [40] and presented the dynamic coefficients of the FPJB at higher unit load conditions (1–2.2 MPa). Vannini et al. [42] measured dynamic and static performances of the FPJB applied to large compressors. The measured results were compared with prediction models and showed good agreement. Early studies [43–46] employed an equivalent stiffness to model the FPJB for radial, tilting, and translational motions of the pad pivot. Suh and Palazzolo [47] presented a full FEM approach to represent the flexure pad-pivot motions. FPJB gas bearings were modeled in Refs. [48,49] using equivalent radial stiffness. Simplified models were employed to consider the thermal characteristics of rotor and bearing. The effect of the pivot's radial stiffness on the TPJB's performance was investigated in Ref. [50], where they compared the pivot stiffness obtained from the theoretical model with measurement.

The paper provides an in-depth development for the numerical modeling of FPJB's and a study of the influence of parameters on ME instability. In Sec. 2, a high-fidelity solution algorithm for the ME was developed by the author's research group in Refs. [19–25], and a thermal-elastohydrodynamic modeling approach for FPJBs was presented by the author's group in Ref. [47]. The latter work neglected the thermal effects of the rotor while including fluid film temperature and thermal–structural effects for the bearing/housing. The present work marries these efforts in developing an original methodology for high-fidelity modeling for the ME, in machines using FPJBs. Section 3 validates the present FPJB model by comparison with the experimental results in Refs. [36,37]. Section 4 compares the accuracies of two FPJB models, i.e., (1) a full FEM-based structural/thermal model and (2) an equivalent stiffness-based model. Section 4 also provides a parametric investigation to illustrate the effects of the FPJB design on ME occurrence. The impact of web thickness on the ME speed range and severity is investigated with the full FEM-based model. The high-fidelity, nonlinear transient ME simulation model is also employed to investigate the effect of bearing supply oil temperature, bearing radial clearance, rotor overhung mass, bearing material, and housing thickness on the ME.

2 Modeling of the Flexure Pivot Bearing and Thermal Shaft

A finite element model of flexure pivot pad is shown in Fig. 1(*a*). Mesh sizes of $21 \times 7 \times 5$ (circumferential, axial, and radial directions, respectively) are employed for pad structures, and $5 \times 7 \times 5$ meshes are used for the web region. The ME simulation with two times the mesh sizes is compared to the results with the current mesh sizes, and no noticeable difference was found in the comparison.

The thickness and length of the flexure web are illustrated in Fig. 1(*b*), and the boundary conditions applied on the pads are also illustrated in Figs. 1(*c*) and 1(*d*). The pressure distributions obtained from the Reynolds equation are applied at the pad's top surface, as shown in Fig. 1(*c*). A rigid bearing housing is assumed, and therefore, a fixed boundary condition is imposed on the bottom surface of the web as shown in Fig. 1(*d*). The pressure distribution condition applied on the top surface is obtained by solving the generalized Reynolds equation and energy equation for the film pressure and temperature

$$\nabla \cdot (C_1 \nabla P) + \nabla C_2 \cdot U + \partial h/\partial t = 0$$

$$C_1 = \int_0^h \int_0^z (\xi/\mu) d\xi dz - C_2 \int_0^h (\xi/\mu) d\xi \tag{1}$$

$$C_2 = \int_0^h \int_0^z (1/\mu) d\xi dz \Big/ \int_0^h (1/\mu) d\xi$$

$$\rho c \left(u \frac{\partial T}{\partial x} + w \frac{\partial T}{\partial z} \right) = k \left(\frac{\partial^2 T}{\partial x^2} + \frac{\partial^2 T}{\partial y^2} + \frac{\partial^2 T}{\partial z^2} \right) + \mu \left[\left(\frac{\partial u}{\partial y} \right)^2 + \left(\frac{\partial w}{\partial y} \right)^2 \right] \tag{2}$$

where h is the fluid film thickness, μ is a lubricant viscosity, ρ, c, and k are density, heat capacity, and conductivity of the film, respectively. In Eq. (1), the surface velocity is U and equals $R\omega$ where R and ω are the journal radius and angular velocity, respectively. The variables x, y, and z in Eq. (2) are the film's circumferential, radial (film thickness direction), and axial coordinates, respectively, and u w are the fluid film velocities in the circumferential and axial directions, respectively.

A viscosity–temperature relation is employed that couples the Reynolds and energy equations:

$$\mu = \mu_0 \exp^{-\alpha(T - T_0)} \tag{3}$$

where μ_0 and T_0 are viscosity and temperature reference values, respectively, α is a viscosity coefficient, and T is film temperatures from the 3D energy equation in Eq. (2). The calculation of the energy equation is conducted using fluid velocities obtained from Eq. (1), and the updated viscosity in Eq. (3) is estimated from the film temperature. In the next calculation step, Reynolds Eq. (1) utilizes the updated viscosity to obtain the new pressure distribution of the film.

The dynamic equations of the pad-flexure web's elastic deformation can be expressed as

$$M_{brg} \ddot{X}_{brg} + K_{brg} X_{brg} = F_{brg} \tag{4}$$

where M_{brg} and K_{brg} are mass and stiffness matrices obtained from the finite element model in Fig. 1, X_{brg} is the vector of elastic deformation, and F_{brg} is the applied nodal force on the pad's top surface.

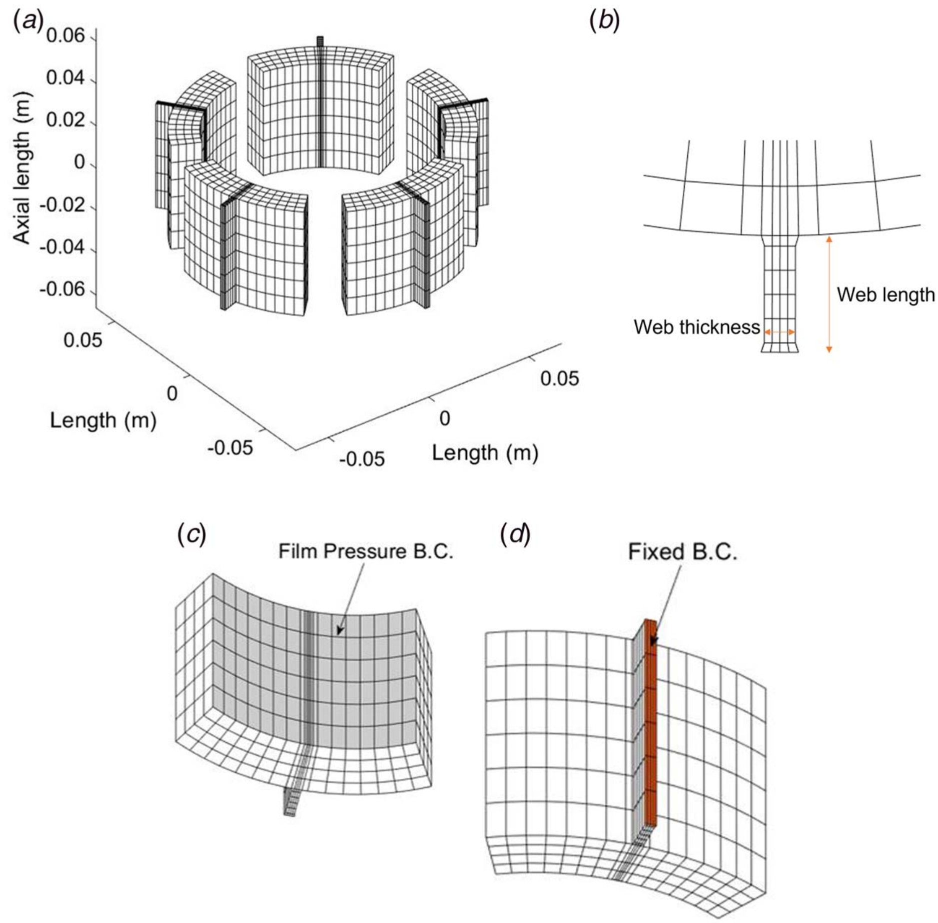

Fig. 1 Structure model of flexure pivot bearing: (*a*) full bearing structural model, (*b*) illustration of pivot dimensions, (c) boundary condition 1 on pad, and (*d*) boundary condition 2 on pad

The dynamic equations in Eq. (4) are diagonalized employing modal orthogonality to accelerate the nonlinear transient solution, and the resulting equations of motions are

$$\Phi_{brg}^T M_{brg} \Phi_{brg} \ddot{Z}_{brg} + \Phi_{brg}^T K_{brg} \Phi_{brg} Z_{brg} = \Phi_{brg}^T F_{brg}$$

$$X_{brg} = \Phi_{brg} Z_{brg} \tag{5}$$

where Z_{brg} and Φ_{brg} are the modal displacement vector and eigenvector matrix, respectively.

The authors in Ref. [47] conducted a sensitivity study to identify the number of eigenmodes that ensures accurate prediction of FPJB performance. The study showed that more than five modes provided a converged result for the full model, and therefore, only the lowest ten eigenmodes of the pad-web structure are employed for the nonlinear transient simulations.

The film thickness equation in Ref. [47] considering the flexibility of the pad is used in the current study, and it is represented as

$$h_n = \sqrt{(x_n - x_s)^2 + (y_n - y_s)^2} - R_n \tag{6}$$

where (x_n, y_n) and (x_s, y_s) are nodal positions on the pad's top surface and journal positions, respectively.

A flexible beam rotor model is also included and coupled with the FPJB model. Equation (7) represents the diagonalized models of the Euler beam utilizing biorthogonality with the right eigenvector ψ_R and left eigenvector ψ_L of the matrix $[D]$

$$[\dot{Y}] = [A][Y] + [\psi_L^T][F] \tag{7}$$

where $[Y] = [\psi_R][U]$, $[A] = [\psi_{Lm}^T][D][\psi_{Rm}] = \begin{cases} \lambda_i \, if \, m = n \\ 0 \, if \, m \neq n \end{cases}$. λ_i is the ith eigenvalue of the system. Modes five times larger than spin speed are ignored to reduce the computational load. The accuracy of the mode number selections on nonlinear ME simulations is validated in Ref. [29].

The coupled dynamic equations of the FPJB in Eq. (5) and the rotor in Eq. (7) are numerically integrated with MATLAB ODE 45 while the fluid load on pads and force applied on the shaft are calculated from Eqs. (1)–(3).

Figure 2 shows the locations of the thermal bearing and shaft models which are explained in this section. Temperature and heat flux continuity are imposed at the shaft/film/bearing interfaces, while iteratively solving the energy equation in the coupled bearing, film, and shaft domains. Convection boundary conditions are imposed on all interfaces with the ambient environment.

A finite element model of an FPJB's thermal model is shown in Fig. 3. The gap between the pad's bottom surface and housing is filled with oil lubricant as illustrated in Fig. 3(*b*), and the temperature of the film in the region is assumed to be constant. Material properties of the oil are applied to the film region while housing material properties are employed for other regions.

The thermal shaft model is illustrated in Fig. 4. At the center region of the shaft (film interface), the temperature of the fluid film calculated by the energy equation in Eq. (2) is assigned as shown in the figure. The total length of the thermal shaft is set to seven-time the axial journal length, and this is selected by gradually increasing the length until the thermal gradient at the axial surface becomes zero. There are two outer surfaces and two axial surfaces in the shaft model, and convection with air is assumed at those surfaces with the convection coefficient of 200 W/m^2.

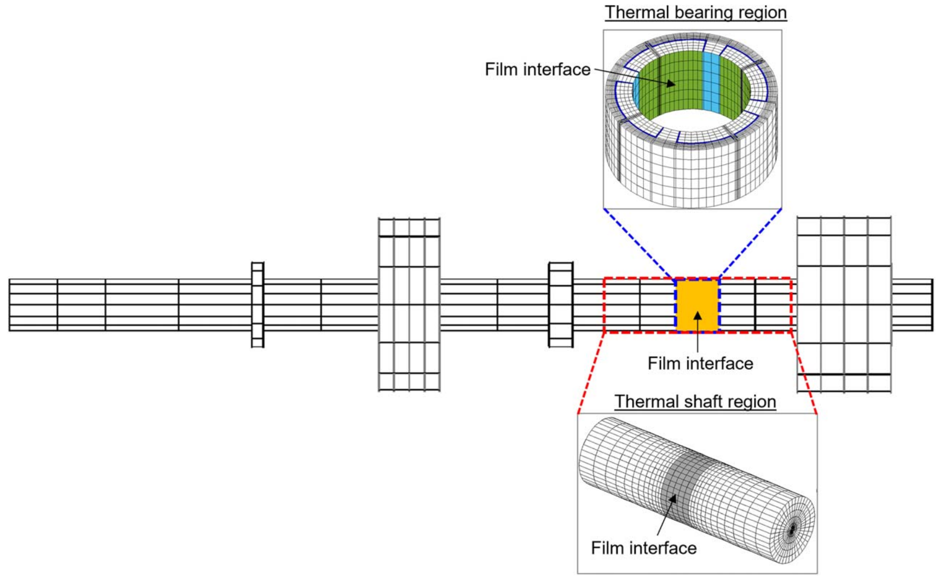

Fig. 2 Thermal bearing/shaft submodel embedded in the overall rotating assembly model

The Laplace equation is solved to obtain the temperature distribution on the bearing and shaft

$$\frac{\partial^2 T}{\partial x^2}+\frac{\partial^2 T}{\partial y^2}+\frac{\partial^2 T}{\partial z^2}=\frac{\rho c}{k}\frac{\partial T}{\partial t} \tag{8}$$

assuming constant thermal conductivity. The discrete form of Eq. (8) is formed utilizing 3D eight-node isoparametric FEM, yielding

$$[C][\dot{T}]+[K][T]=[F] \tag{9}$$

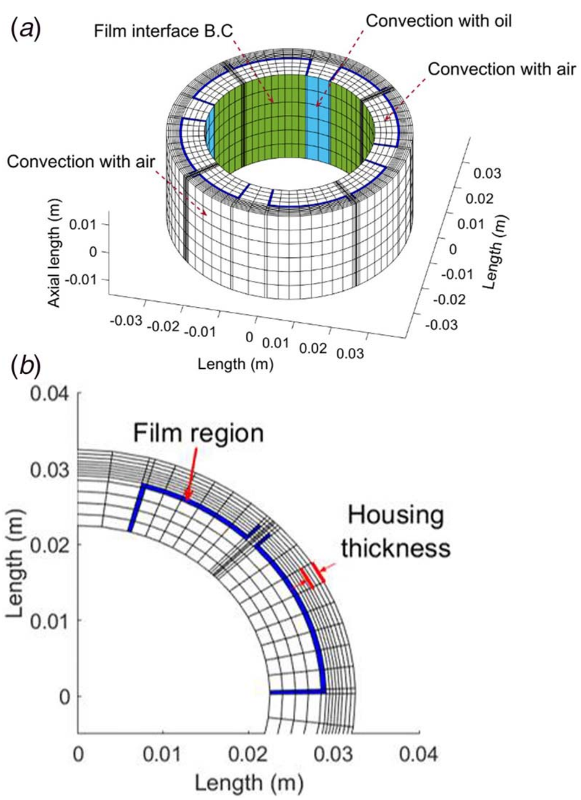

Fig. 3 Thermal models of (*a*) bearing including different thermal boundary conditions and (*b*) axial view of bearing model including fluid film region

where F is the time-varying thermal load updated with the physical states of the rotor-bearing system

The transient solution of Eq. (9) is obtained via numerical integration using MATLAB ODE 45. The dynamic equations of FPJB and rotor in Eqs. (4)–(7), and thermal models in Eq. (9) are systematically coupled and solved with nonlinear transient simulation schemes. Details of the ME algorithms and solution procedures are explained in the Refs. [20–25], and a brief summary of the process is provided here. Film temperature is obtained at 40 points on the rotor vibration orbit by solving the film energy Eqs. (1) and (2). The film viscosity field is likewise updated at these steps via Eq. (3) and the updated film temperature field. The orbital motion and film temperatures are solved iteratively with Eqs. (1)–(7) until convergence is attained. The bearing and shaft temperature distributions, and thermal bow and thermal expansions of the bearings and shafts are then updated by solving the transient thermal conduction Eqs. (8) and (9), and structural equilibrium equations. A detailed presentation of this procedure is given in Ref. [22].

Note that the staggered time integration scheme in Refs. [20–25] is employed for the shaft/bearing thermal calculations for improved computational efficiency. The obtained temperatures and bow/expansion affect the thermal boundary conditions on the film and film thickness, which are utilized in the successive calculation step. The iterative processes among dynamic equation, energy/Reynolds equation, temperature, and thermal bow/expansion calculations are conducted until the ME vibration occurs or the specified simulation time is reached.

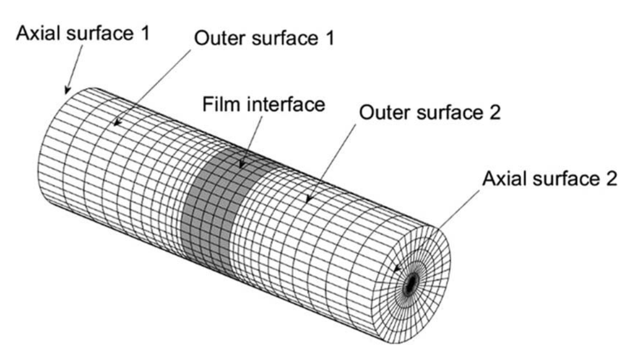

Fig. 4 Sub-boundaries for thermal boundary condition specification

Table 1 Rotor and bearing parameters for verification case [36,37]

Lubricant parameters		FPJB parameters	
Viscosity at 50 °C (Ns/m^2)	0.0203	Pad type	Load between pads (LBP)
Viscosity coefficients (1/°C)**	0.031	No. pads	4
Supply temperature (°C)	30	Radius of shaft (m)	0.0225
Inlet pressure (Pa)	1.1×10^5	Bearing clearance (μm)	50
**In exponential μ versus T law		Preload	0.33
		Bearing length (m)	0.03
Shaft parameters		Thermal expansion coefficient (1/°C)	1.7×10^{-5}
Heat capacity (J/kg °C)	453.6	Reference temperature for thermal expansion	25 (°C)
(Heat conductivity (W/mK)	50	Web thickness	0.75 mm
Thermal expansion COEFF (1/°C)	1.22×10^{-5}	Web length	2.5 mm
Reference temperature for thermal expansion	25 (°C)	Housing thickness (m)	0.0175
Thermal rotor length (m)	0.21		
		Linear ball bearing	
		K_{xx}, K_{yy} (N/m)	3×10^8
		C_{xx}, C_{yy} (Ns/m)	10

3 Model Validation

The ME prediction model for the rotor with the FPJB is validated with an experimental observation from Refs. [36,37]. In the reference, the flexible rotor with FPJB at the non-drive end (NDE) side encountered the ME phenomenon along with large spiral vibrations and high journal temperature differential (ΔT) at 6550 rpm and 6850 rpm. The rotor and bearing parameter values are presented in Refs. [36,37] and Table 1.

For the film region, a heat capacity of 2000 J/kg °C and heat conductivity of 0.13 W/mK are applied, while a heat capacity of 453 J/kg °C and heat conductivity of 50 W/mK are used for the bearing pad/web/housing regions. At the outer and axial surfaces of the bearing, convection from air conditioning is imposed with the convection coefficient of 200 W/m^{2}K. At the inner surfaces of the bearing, both film temperature and convection with oil conditions are imposed depending on the locations. The coefficient for oil convection is assumed to be 300 W/m^{2}K. Note that the bearing material of the FPJB in Refs. [36,37] is bronze with Young's modulus of 1.15×10^{11} Pa and thermal expansion coefficient of 1.7×10^{-5} (1/°C). These values are applied for both the critical speed calculation and the ME simulations in this work.

Twice the imbalance magnitude from the reference was employed in the current simulations since the Morton effect did not occur in the simulation with the reported value. The imbalance may have a large uncertainty due to the unknown residual imbalance. In the reference, the critical speed of the rotor is predicted at around 7300 rpm. However, as shown in Fig. 5, the predicted critical speed of the current simulation using the full FPJB model is calculated at 7780 rpm, which is about 500 rpm higher than the prediction in Refs. [36,37]. A predicted Morton effect was not observed at the supply oil temperature of 22 °C, corresponding with the experimentally observed Morton effect in Refs. [36,37]. A Morton effect was predicted when the supply oil temperature was raised to 30 °C in the present simulation. The simulation inlet supply pressure was the same as the experimental value of 1.1 bar. Raising the inlet oil supply temperature from 22 °C to 30 °C increased the predicted critical speed from 7728 rpm to 7780 rpm. Both of these values are approximately 6.5% higher than the predicted critical speed of 7300 rpm in Refs. [36,37]. This discrepancy may be attributed to the manufacturing errors in bearing clearance, preload measurement and housing flexibility, unmodeled dynamics (oil mixing and solid shaft model based on 3D FEM) in the current model, and uncertainties in the parameters used for the current study.

Spiral vibrations with a high journal temperature differential little less than 10 °C were observed in Refs. [36,37] at 6550 rpm. In the current simulation spiral vibration and high journal ΔT was observed at 7450 rpm as shown in Fig. 6. It is known that most ME cases occur near the first bending mode of the rotor-bearing system. Since the predicted critical speed of the current study was higher than the experiment in Refs. [36,37], the ME speed range may also be shifted up in accordance with the critical speed change. The maximum journal ΔT of 8.6 °C occurs after 1 min with the full FPJB model, and this value is slightly less than the maximum value in the experiment [36,37]. Similar to the experiment, an instability caused by rubbing is observed. This occurred in the simulation at 7550 rpm.

4 Parametric Study

Parametric studies of FPJB design parameters are conducted with the rotor configuration in Ref. [8]. The rotor in Ref. [8] is a single overhung type rotor supported by a TPJB at its NDE side. To test

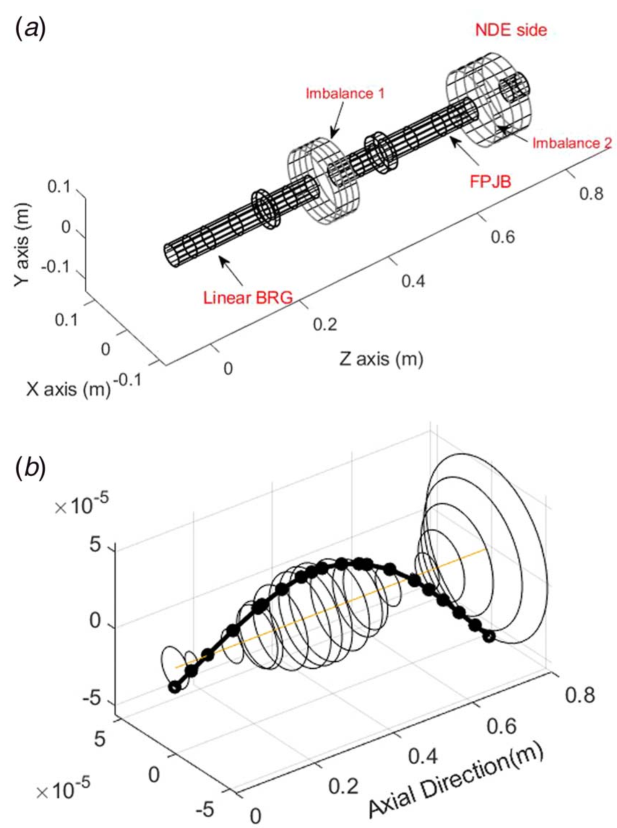

Fig. 5 (a) Outline of the flexible rotor with FPJB in Refs. [36,37], and (b) mode shape of rotor at the critical speed (7780 rpm; damping ratio, 0.1)

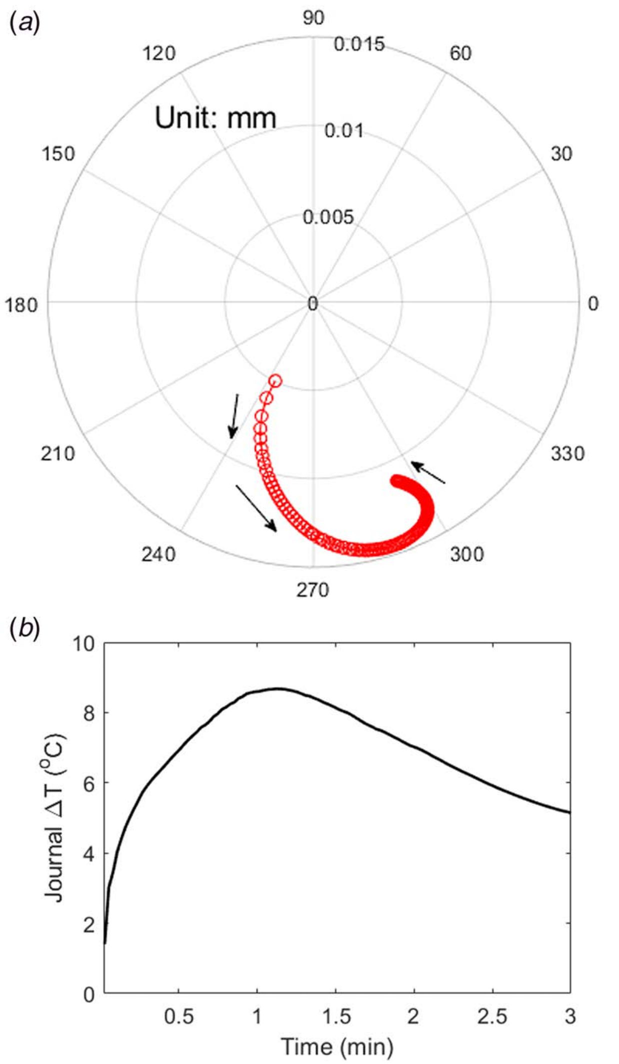

Fig. 6 Simulation results at 7450 rpm: (*a*) 1× polar plot and (*b*) journal temperature differential

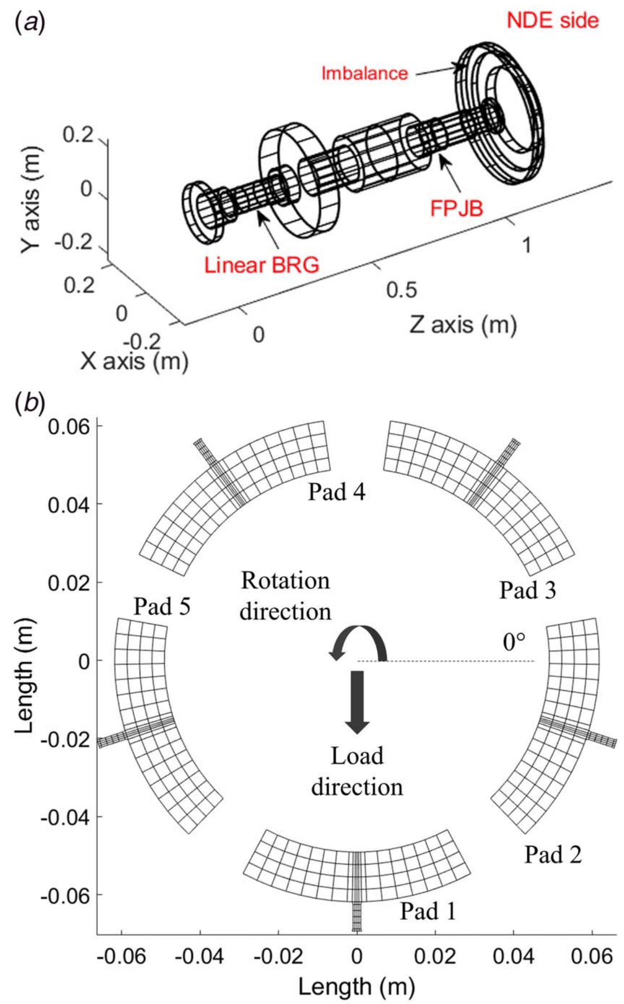

Fig. 7 (*a*) Rotor outline with FPJB and (*b*) FPJB + rotating direction

the FPJB design impacts, the TPJB is replaced with the FPJB from the reference model. The position of the bearing is identical to the original location of the TPJB. The single overhung rotor with an FPJB used for the current study is illustrated in Fig. 7(*a*). The rotor, bearing, and lubricant parameters are also listed in Table 2. The web thickness and length of the FPJB are assumed to be 1.5 mm and 5 mm, respectively. The configuration and bearing dimensions such as radius, length, and clearance are identical to the TPJB model in Ref. [8].

To verify the ME occurrence in the current rotor-FPJB system, preliminary simulations with and without thermal bow effect are presented in Fig. 8. For the "without thermal bow effect" case, the induced thermal bow amplitude is set to zero. Nonlinear steady-state vibrations for both cases at the bearing location are presented in Fig. 8(*a*). Since the vibrations along with the ME

Table 2 Rotor and bearing parameters

Lubricant parameters		FPJB parameters	
Viscosity at 50 °C (Ns/m^2)	0.0203	Pad type	LOP
Viscosity coefficient (1/°C)**	0.031	No. pads	5
Supply temperature (°C)	50	Radius of shaft (m)	0.0508
Inlet pressure (Pa)	1.32×10^5	Bearing clearance (μm)	74.9
** In exponential μ versus T law		Preload	0.5
		Bearing length (m)	0.0508
Shaft parameters		Thermal expansion coefficient (1/°C)	1.3×10^{-5}
Heat capacity (J/kg °C)	453.6	Reference temperature for thermal expansion	25 (°C)
Heat conductivity (W/mK)	50	Web thickness	1.5 mm
Thermal expansion coefficient (1/°C)	1.22×10^{-5}	Web length	5 mm
Reference temperature for thermal expansion	25 (°C)	Housing thickness	4 mm
Thermal rotor length (m)	0.3508		
		Linear ball bearing	
		K_{xx}, K_{yy} (N/m)	1.7×10^8
		C_{xx}, C_{yy} (Ns/m)	1.0×10^5

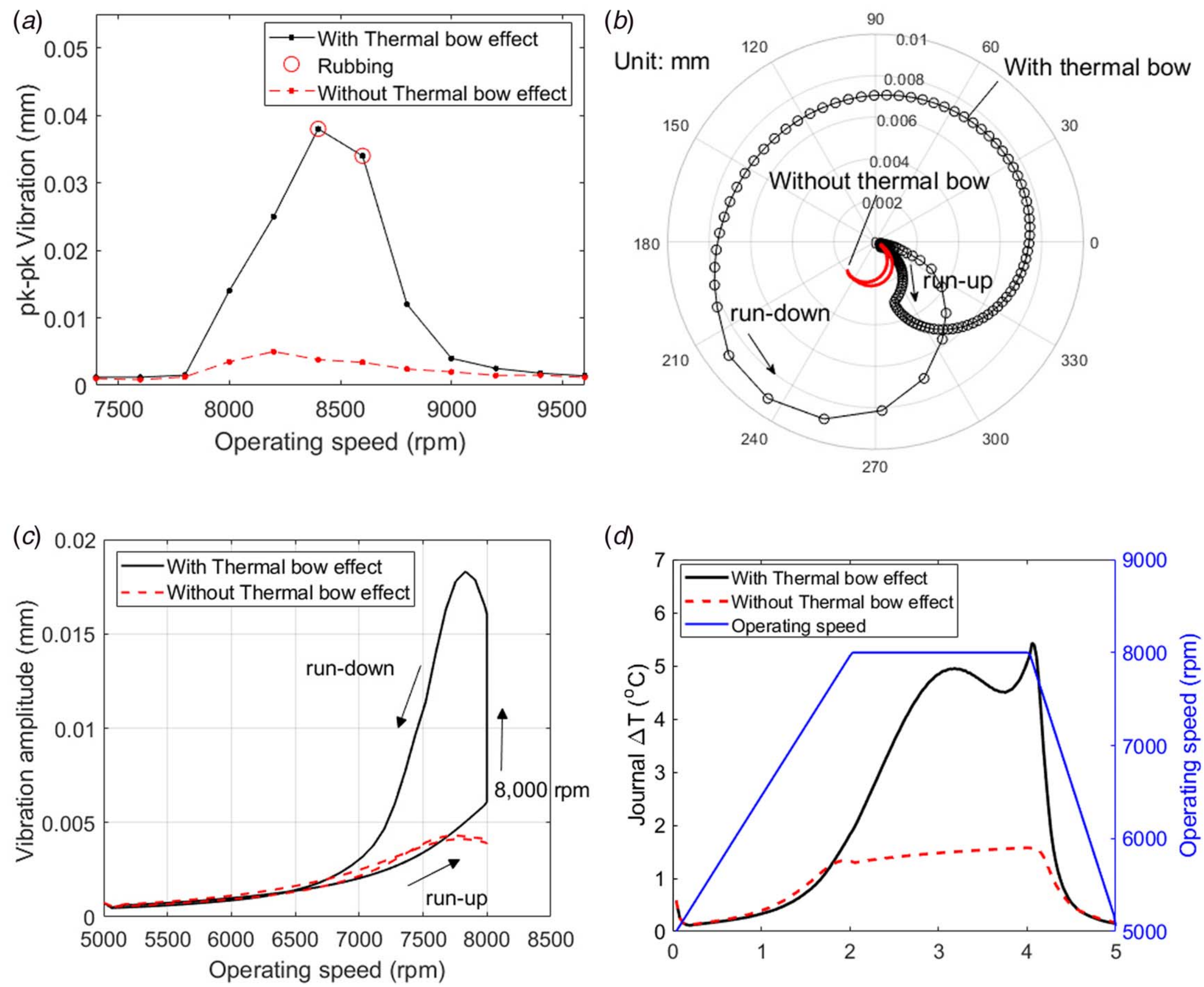

Fig. 8 Nonlinear steady-state vibration level with and without thermal bow effect: (*a*) vibration amplitude at bearing location with different speeds, (*b*) 1× polar plot (run-up/down operation, from 5000 rpm to 8000 rpm), (*c*) vibration amplitude during run-up/down operation (hysteresis plot), and (*d*) journal ΔT during run-up/down operation

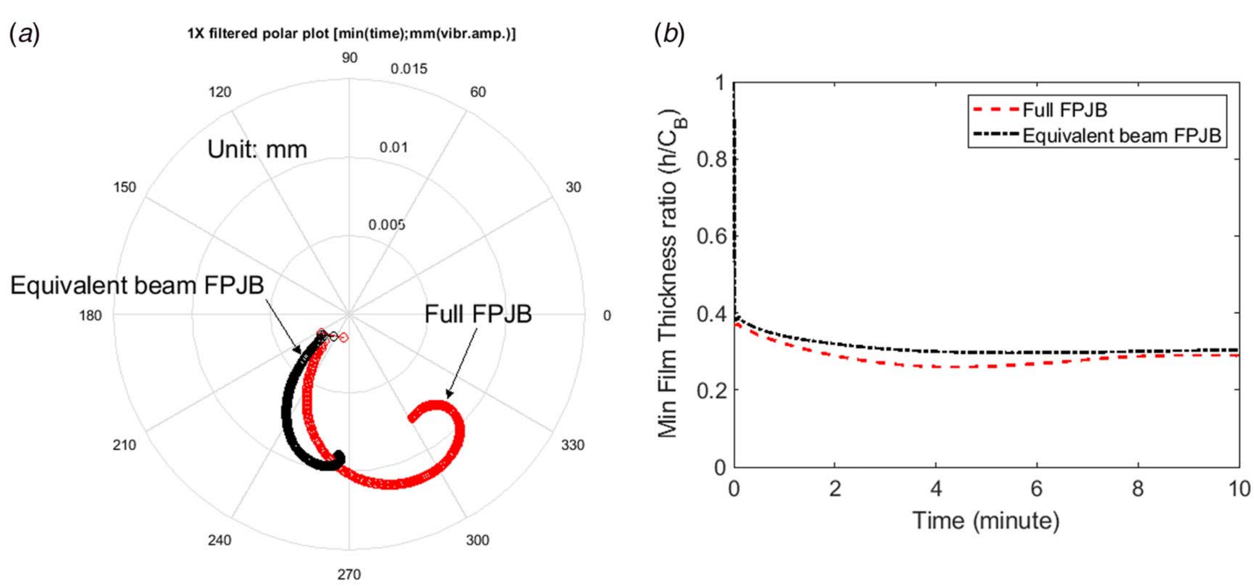

Fig. 9 (*a*) 1× polar plot and (*b*) minimum film thickness ratio at 7800 rpm

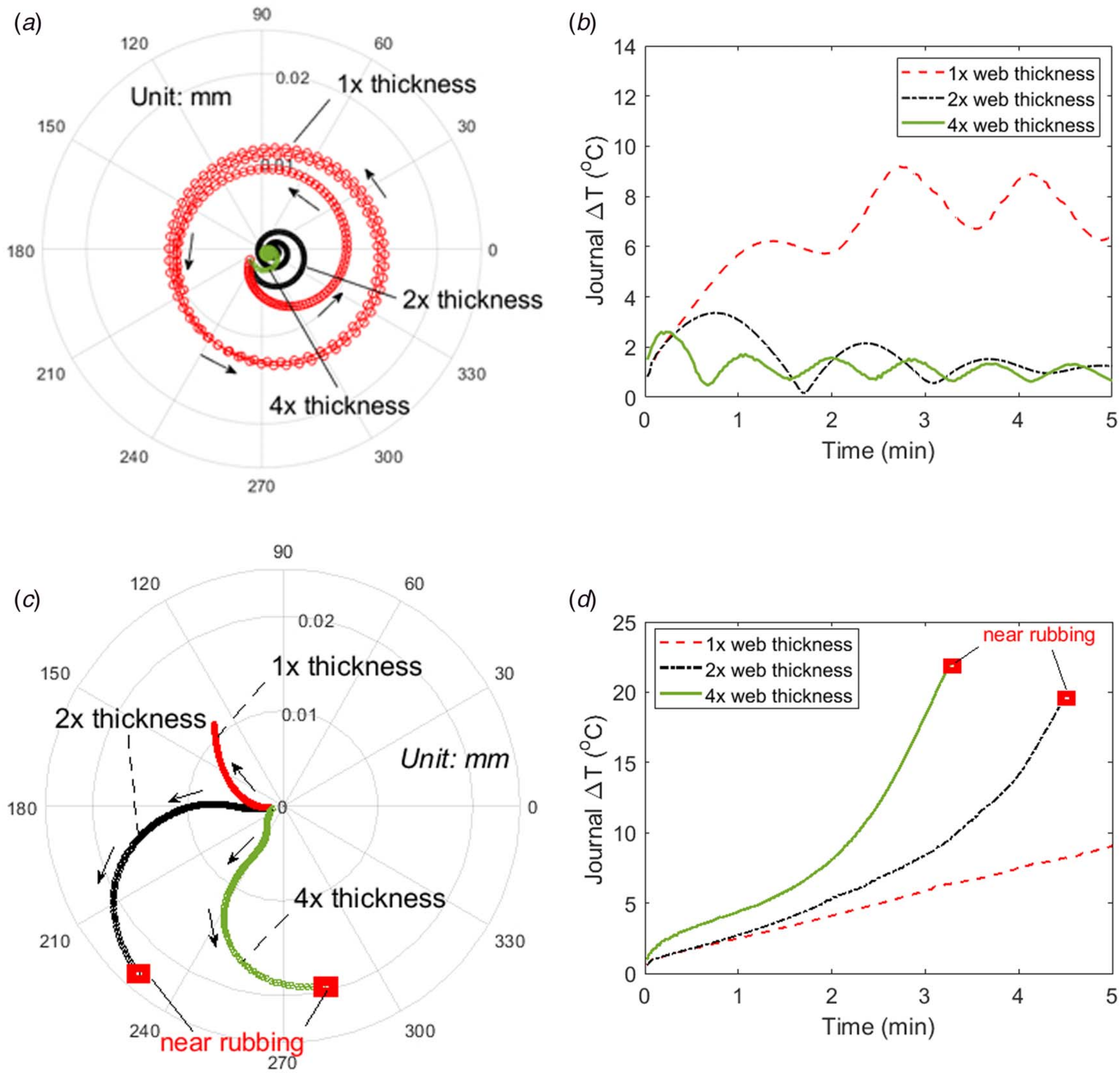

Fig. 10 Vibration and temperature responses with different web thicknesses: (*a*) 1× polar plot at 8000 rpm, (*b*) journal ΔT at 8000 rpm, (*c*) 1× polar plot at 8800 rpm, and (*d*) journal ΔT at 8800 rpm

phenomenon often encounter the non-converging or diverging vibration, the "steady-state vibration' is defined to be the maximum vibration level for 5 min of simulation time for the non-converging case. For the diverging vibration case, a near rub condition is assumed to occur when the minimum film thickness of the bearing becomes less than 5% of the nominal bearing clearance, and the simulation is stopped. The result shows that much higher vibration level with the "with thermal bow case" (black line) compared to the "without thermal bow case" (dotted line).

Two distinct characteristics of the rotor experiencing the ME are the spiral vibration in the 1× polar plot and clear hysteresis during run-up/down operation. The spiral vibrations and hysteresis plots of both with and without thermal bow are compared in Figs. 8(*b*)–8(*d*). A 1× polar plot during run-up/down operation is shown in Fig. 8(*b*), where the speed increases from 5000 rpm to 8000 rpm in 90 s, dwells at 8000 rpm for 120 s, and then decelerates back to 5000 rpm in 45 s. This figure also shows a much larger spiral-shaped-vibration when a thermal bow is included, confirming the presence of the ME. The ME is also confirmed by the hysteresis plot in Fig. 8(*c*), which corresponds to the same speed schedule as shown in Fig. 8(*d*). Note that the hysteresis phenomenon occurs in the rotor encountering the ME because the time scale of the thermal response is normally much larger than that of structural/dynamic responses. The figure shows that the vibration amplitude keeps increasing at the constant operating speed when the thermal bow effect is included. The vibration level during the run-down is also much larger than the vibration of the run-up which is also observed in the case history in Ref. [32] and experiment in Refs. [36,37]. Note that without the thermal bow effect, the vibration amplitude between run-up and run-down is almost identical to each other in Fig. 8(*c*). The journal ΔT plots during the run-up/down are shown in Fig. 8(*d*), which shows that much higher journal ΔT is induced for the thermal bow case indicating the hysteresis phenomenon is caused by the thermal bow.

4.1 Equivalent Pivot Stiffness FPJB Model. In Fig. 9, an equivalent pivot stiffness-based FPJB model employing estimated radial and tilting stiffness of the FPJB's web is compared to the full FPJB model in black line. The radial and tilting stiffness of

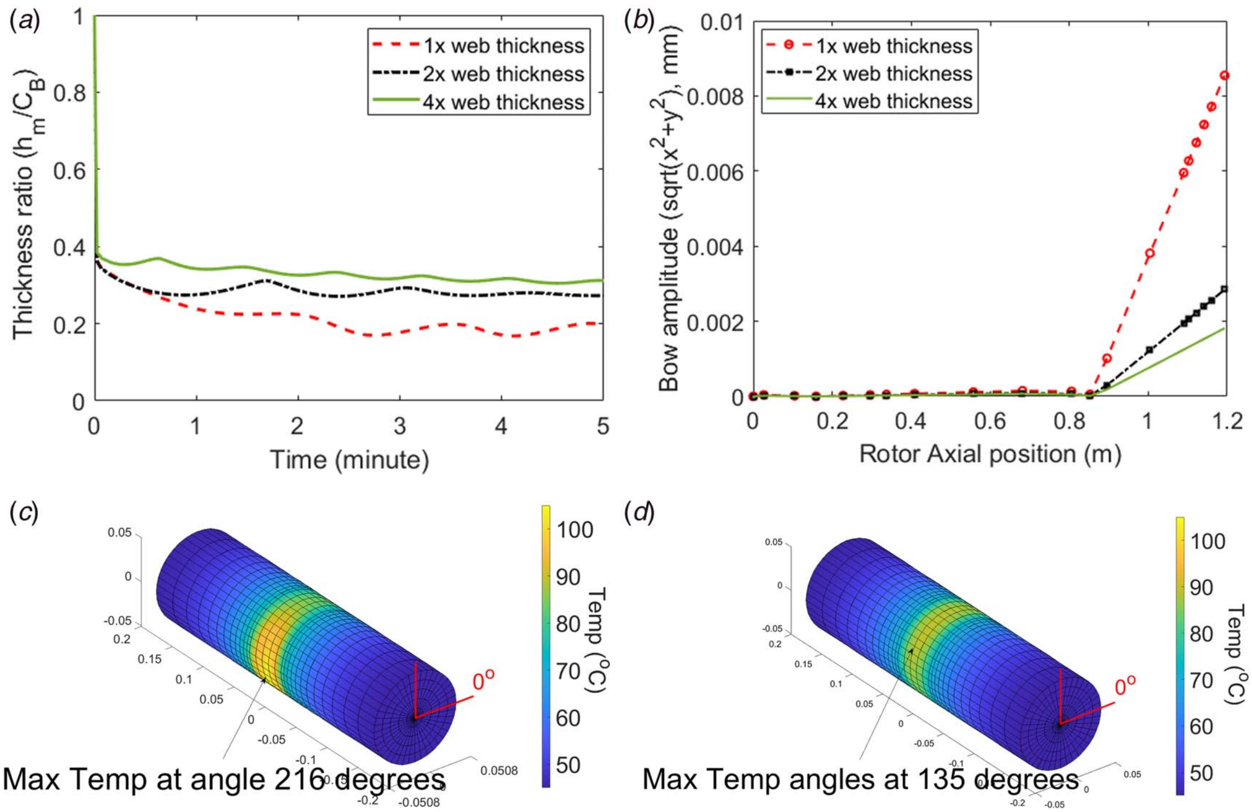

Fig. 11 Simulation results at 8000 rpm with different web thickness: (*a*) film thickness and (*b*) amplitude of bow at the end of simulation, (*c*) maximum shaft temperature of 1× thickness, and (*d*) maximum shaft temperature of 4× thickness. Dimensions in meters.

the web can be obtained from a beam theory [37], and it is represented as

$$K_{eq} = \begin{bmatrix} \frac{AE}{L} & 0 & 0 \\ 0 & \frac{12EI}{L^3} & -\frac{6EI}{L^2} \\ 0 & -\frac{6EI}{L^2} & \frac{4EI}{L} \end{bmatrix} \tag{10}$$

where A, E, L, and I are pivot area, Young's modulus of pivot, pivot length, and pivot's moment of inertia, respectively

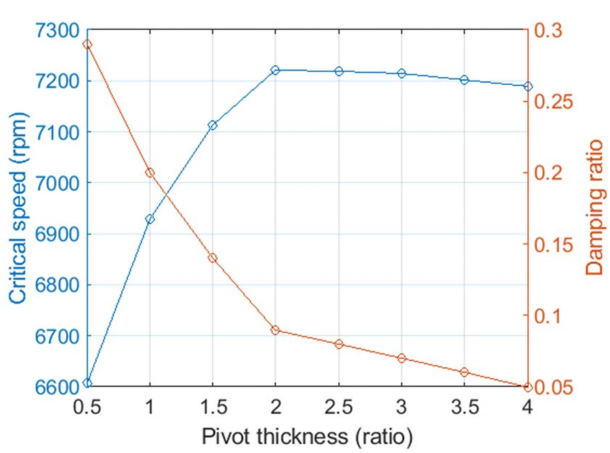

Fig. 12 Critical speed and damping ratio (obtained from the solid model)

The first, second, and third rows of K_{eq} the matrix correspond to the web's radial, transverse (tangential), and tilting motions, respectively. The radial stiffness of 3.20e9 N/m and the tilting stiffness of 2835 Nm/rad are obtained from the current pivot geometries in Table 2. These stiffness values are applied to the tilting pad bearing model accounting for web's radial and tilting motions for the equivalent FPJB model.

Then, the equations of motion for the equivalent FPJB model are

$$I_{radial\_i}\, \ddot{y}_{pvt\_i} = F_{pad\_i} - K_{eq_{(1,1)}}\, y_{pvt\_i}$$

$$I_{trans\_i}\, \ddot{\delta}_{trans\_i} = M_{trans\_i} - K_{eq_{(2,2)}}\, \delta_{trans\_i} - K_{eq_{(2,3)}}\, \delta_{trans\_i}$$

$$I_{tilting\_i}\, \ddot{\delta}_{tilting\_i} = M_{tilting\_i} - K_{eq_{(3,2)}}\, \delta_{tilting\_i} - K_{eq_{(3,3)}} \delta_{tilting\_i} \tag{11}$$

where i represents the pad number, I_{radial_i}, I_{tran_i}, and $I_{tilting\_i}$ are the mass and the translational and tilting inertias of each pad, respectively, and F_{pad_i}, M_{trans_i}, and $M_{tilting\_i}$ represent the fluid film force and the translational and tilting moments applied to each pad, respectively.

The equivalent FPJB model used here is similar to the TPJB models in Ref. [27] except that the current model additionally includes the tilting stiffness of the pads.

Here, translational (perpendicular to pivot's radial motion) stiffness of the pivot is neglected because the maximum translational pad deflection is very small compared to the other motions due to very small film clearance as demonstrated in Ref. [48]. To demonstrate this assumption, a nonlinear Morton effect simulation was conducted with and without the coupling effect between tilting and translational motions of the pivot, and the results showed almost identical results.

In Figs. 9(*a*) and 9(*b*), the equivalent model is compared with the full FPJB model (FEM-based), and the equivalent model somewhat

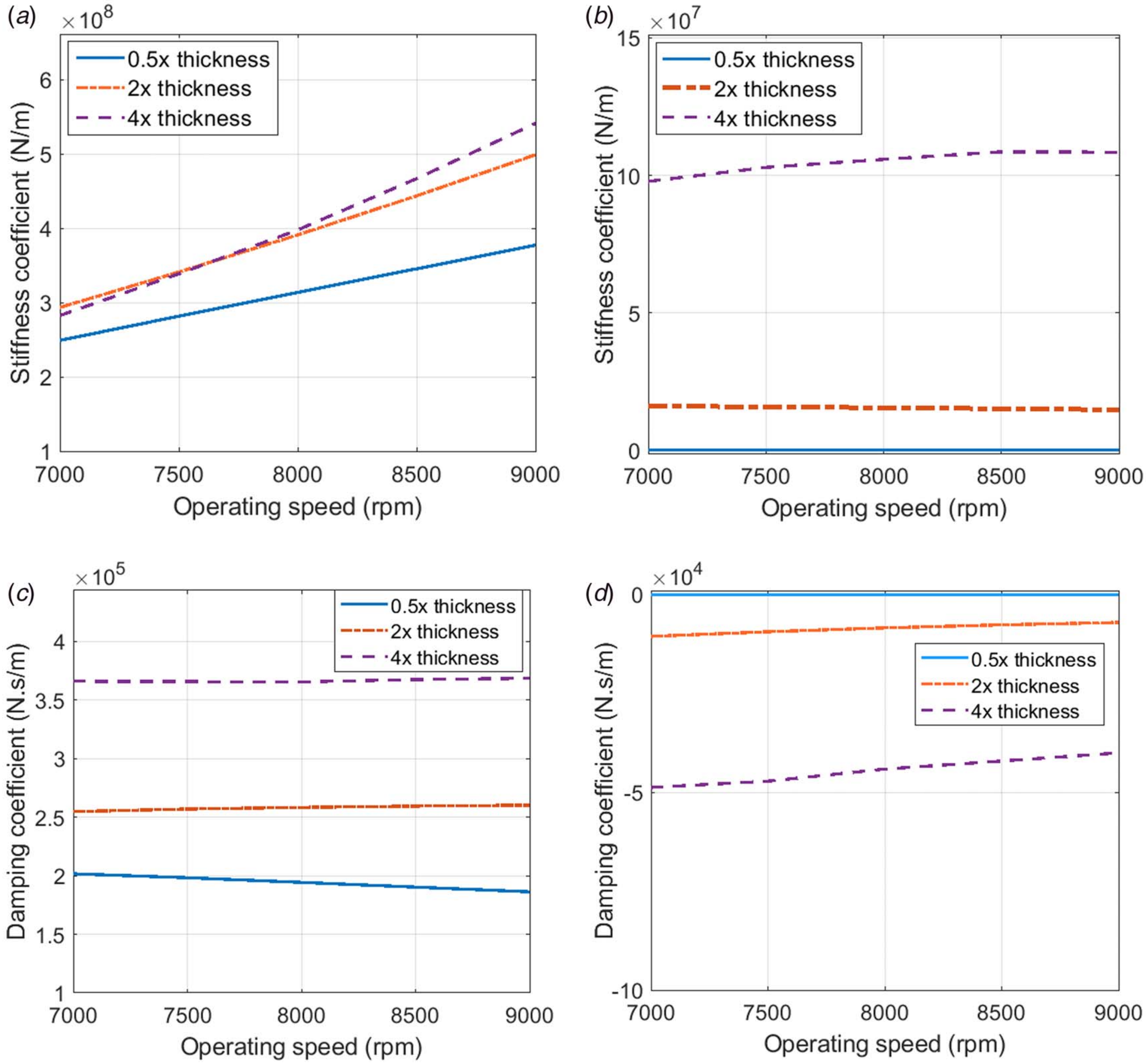

Fig. 13 **(*a*) FPJB stiffness coefficients (K_{xx}), (*b*) FPJB stiffness coefficients (K_{xy}), (c) FPJB damping coefficients (C_{xx}), (*d*) FPJB damping coefficients, and (C_{xy}) (obtained from solid model)**

underpredicts the ME vibration as shown in the simulation result at 7800 rpm, as demonstrated by smaller spiral vibration and larger minimum film thickness ratio. For the following simulations, the full FPJB model including finite element (FE) thermal/structural models will be used to investigate design effects.

4.2 Effect of Varying Web Thickness. To investigate the impact of web thickness on the ME vibration, the thickness values are varied from 1.5 mm (1× thickness) to 6 mm (4× thickness), and its simulation results are shown in Fig. 10. Journal ΔT in Figs. 10(*b*) and 10(*d*) indicates the difference between the maximum and minimum temperatures at journal circumference. Note that Figs. 10(*a*) and 10(*b*) represent the simulation results at 8000 rpm, and (*c*) and (*d*) represent the results at 8800 rpm. Spiral vibration is indicated by the varying amplitude and phase of vibration at a constant operating speed. With 1× thickness at 8000 rpm, clear spiral vibration appears with maximum pk–pk vibration amplitude around 0.012 mm in Fig. 10(*a*). During the 5 min of operation shown, the vibration amplitude does not converge, and the phase of the vibration continuously changes from 0 deg to 360 deg, as indicated by the spiral-shaped trajectory in the 1× polar plot in Fig. 10(*a*). Increasing the web thickness is seen to suppress the vibration amplitudes, as compared to the 1× thickness vibration. The vibration converges to a very small level during the 5 min, with the 4× web-thickness case.

The journal ΔT of the corresponding cases are presented in Fig. 10(*b*). The journal ΔT fluctuates with the maximum value up to 9.4 °C in the 1× thickness, and relatively small journal ΔT is predicted with the thicker 2× and 4× cases in the figure. Opposite trends of vibration and journal ΔT occur at 8800 rpm as shown in Figs. 10(*c*) and 10(*d*), where the spiral vibration and journal ΔT increases with thicker webs. The largest spiral amplitude is seen to occur with the 4× thickness in the 1× polar plot in Fig. 10(*c*). The simulations of the 2× and 4× web-thickness cases were stopped before 5 min, because the minimum film thickness dropped below 5% of nominal bearing clearance, indicating near rubbing. The phase lag in Figs. 10(*c*) and 10(*d*) changes from the initial value of 168.3 deg to 131.3 deg for the 2× thickness case, while it shifts from 167.5 deg to 82.5 deg for the 4× thickness case. The phase lag angle of the vibration was calculated relative to the initial imbalance force direction angle of 0 deg. The synchronous instability follows different directions for the 2× and 4× cases as time progresses. This results from the change in bearing

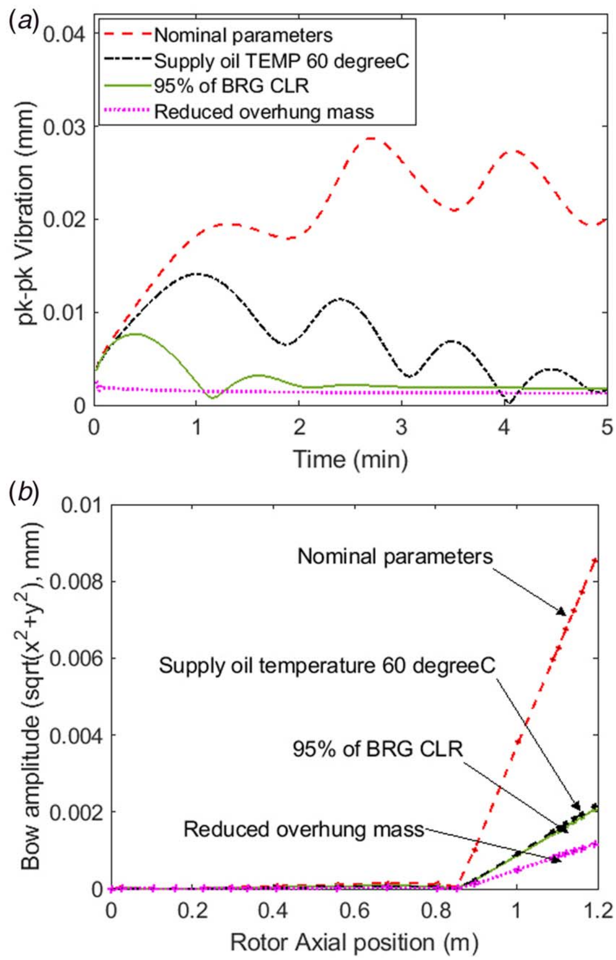

Fig. 14 (*a*) rotor pk–pk vibration amplitude and (*b*) bow amplitudes with different rotor-bearing parameters at 8000 rpm

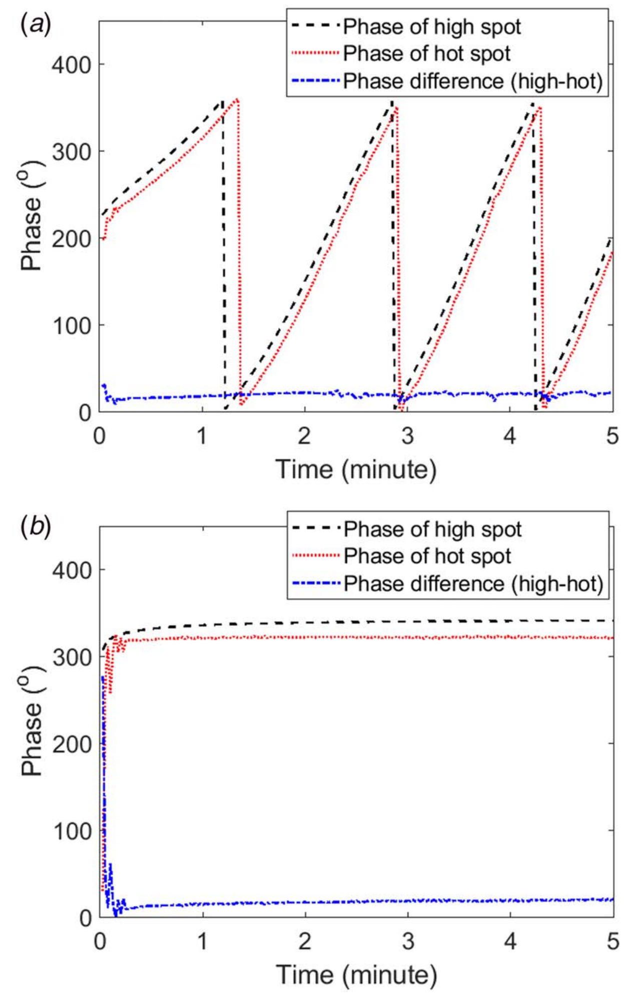

Fig. 15 High spot, hot spot, and difference phase angles for the (*a*) "Nominal parameters" case and (*b*) "Reduced overhung mass" case in Fig. 14

coefficients and critical speeds between the 2× thicknesses, which change the angles between the heavy spot and high spot even without considering the ME. The journal ΔT in Fig. 10(*d*) also shows a similar trend with the spiral vibration. With 2× and 4× web thicknesses, the journal ΔT exceeds 20 °C along with near rubbing conditions around 3 min and 4.5 min, respectively. Near rubbing occurs at vibration amplitudes much less than the radial clearance due to equilibrium eccentricity and shaft and pad growths.

Figure 11 shows the minimum film thickness ratio and thermal bow amplitude distribution at the end of the 5-min simulation, for 8000 rpm with different web thicknesses. Consistent with the smaller vibration and ΔT with thicker webs in Figs. 10(*a*) and 10(*b*), the minimum film thickness tends to increase with thicker webs in Fig. 11(*a*). The thermal bow amplitude in Fig. 11(*b*) is at the end of the 5-min simulation for each case. The smallest thermal bow amplitude is predicted with the 4× thickness case, and this trend explains the relatively small vibration amplitudes with the 4× thickness in Figs. 10(*a*) and 10(*b*). The maximum temperature region on the journal surface for both 1× and 4× web-thickness cases are shown in Figs. 11(*c*) and 11(*d*). The highest journal temperature is seen to occur with the 1x case, leading to increased thermal bow amplitude, vibration level, and journal ΔT.

The linearized dynamic coefficients stiffness and damping are calculated for each web case, and the first bending critical speed is calculated based on conventional rotordynamic analysis in Figs. 12 and 13. Note that the calculated radial and tilting stiffness are presented for the completeness of the work, and the elastic model of FPJB is used for dynamic coefficients calculation.

The critical speeds in Fig. 12 show that the critical speed increases from 6600 rpm to 7280 rpm with thicker webs while the damping ratios decrease with thicker webs. The damping ratio here is defined by $\xi = -\mathrm{real}(\lambda)/|\lambda|$ where λ is the eigenvalue corresponding to the critical speed. Reference [24] shows that the ME speed range shifts as critical speed shifts. Consequently, the ME speed shifts in the current simulation can be explained by the critical speed changes with different web thicknesses. As demonstrated in Ref. [43], changes in the cross-coupled stiffness values, i.e., increasing K_{xy} and decreasing K_{yx}, reduce logarithmic decrements, thus decreasing rotor stability and risking deleterious subsynchronous vibration. FPJB design goals include reducing the rotational stiffness of the pad to decrease K_{xy} and increase K_{yx}, while also reducing the potential for the Morton Effect. Figure 12 shows an increasing trend for damping ratio with decreased pivot thickness, similar to

Table 3 Material properties of steel and bronze

	Bronze	Steel
Young's modulus	1.1e11 Pa	2.15e11 Pa
Poisson's ratio	0.35	0.3
Density	8960 kg/m^3	7850 kg/m^3
Thermal expansion coefficient	1.7e5 (1/°C)	1.22e5 (1/°C)
Heat capacity	385 J/kg °C	453 J/kg °C
Heat conductivity	401 W/mK	50 W/mK

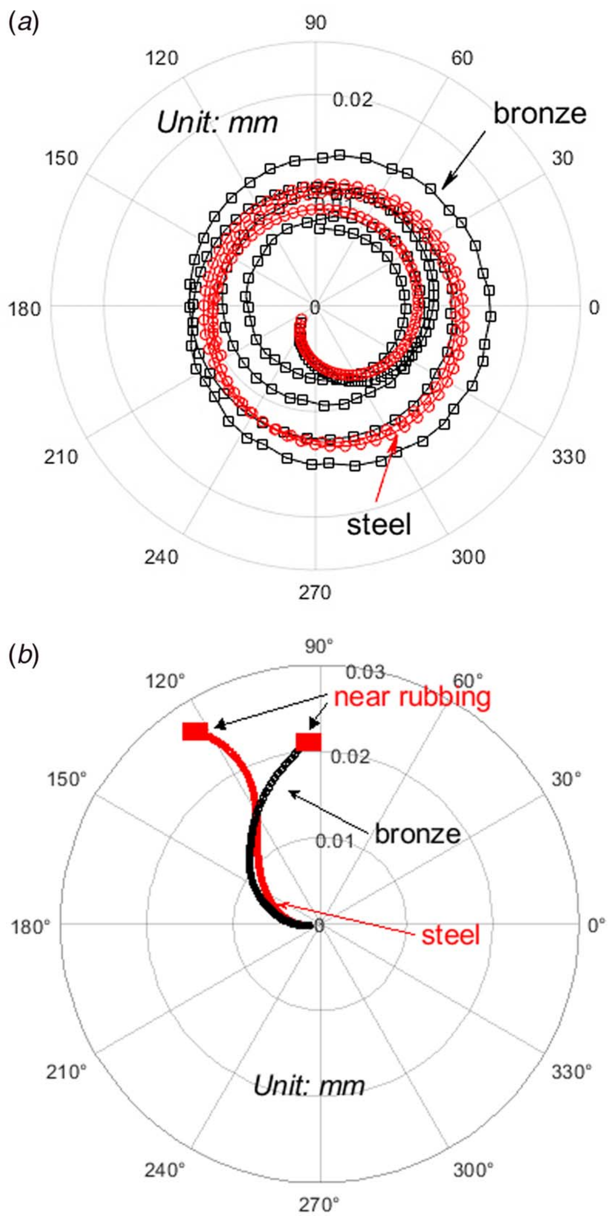

Fig. 16 5 min simulation results with different bearing materials (steel and bronze): (*a*) 1×, p–p vibration polar plot at 8000 rpm and (*b*) 1× polar plot at 8800 rpm

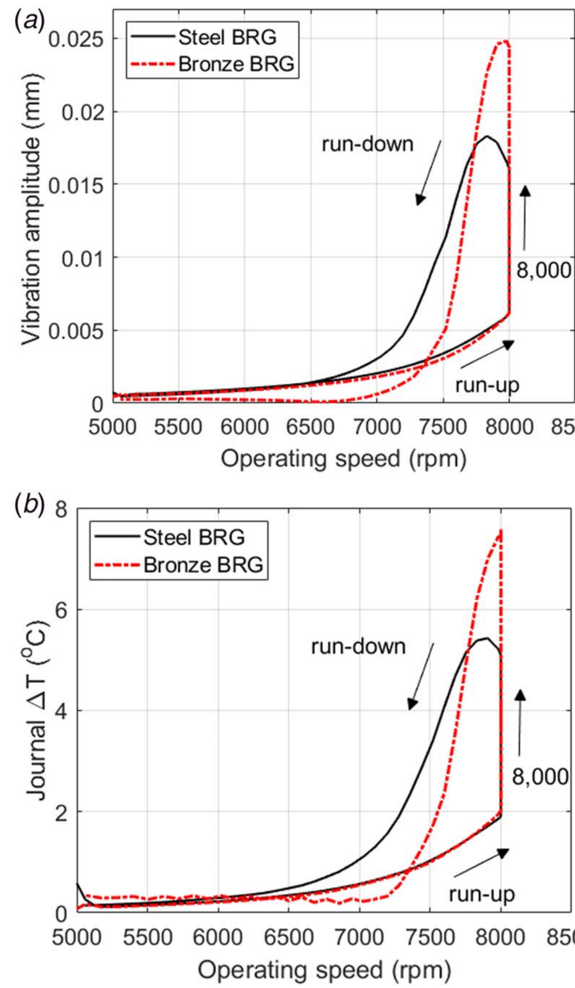

Fig. 17 Bode plots with hysteresis for steel and bronze bearings: (*a*) vibration amplitude at bearing and (*b*) journal Δ*T*

Ref. [43]. This must be considered when adjusting the pivot thickness to reduce the potential for ME occurrence, as demonstrated in Fig. 10.

The stiffness and damping coefficients of the rotor-bearing system are shown in Fig. 13. The principal (K_{xx} and C_{xx}) and cross-coupled stiffness/damping values (K_{xy} and C_{xy}) increase as the web thickness increases. The remaining stiffness and damping values (K_{yy}, K_{yx}, C_{yy}, and C_{yx}) are not presented here because the K_{yy} and C_{yy} values are similar to K_{xx} and C_{xx}, and K_{yx} and C_{yx} have similar amplitude with K_{xy} and C_{xy} but are of opposite signs.

To investigate the effects of the rotor-bearing parameters on ME, bearing supply oil temperature, bearing radial clearance, and rotor overhung mass are varied from its nominal values in Table 2, and its vibration levels and bow amplitude due to the Morton effect at 8000 rpm are compared in Fig. 14. As shown in the figure, a higher supply oil temperature of 60 °C, 5% reduced bearing clearance and 10% reduced overhung mass suppressed the vibration level and induced bow amplitudes. The predicted vibration amplitude variation with parameter changes agreed well with the trends identified in Ref. [24] with regard to shifts in the critical speed and the ME speed range. Increasing the supply oil temperature to 60 °C from the nominal value of 50 °C increased the critical speed from 6929 rpm to 7003 rpm. Decreasing the bearing radial clearance by 5% increased the critical speed to 7256 rpm, and reducing the overhung mass by 10% of its nominal value increased the critical speed to 8815 rpm. The level of ME vibration suppression in Fig. 14(*a*) followed an inverse trend compared with the critical speed shifts, so, for example, the large increase in critical speed with overhung mass reduction caused a large decrease in ME vibration. This is consistent with the trends coupling critical speed and ME identified in Ref. [24]. These results indicate that the measures to remedy the ME applied to the rotor supported by TPJBs can be similarly applied to the rotor with FPJBs.

Figures 15(*a*) and 15(*b*) show the high spot, hot spot, and their different phase angles corresponding to the "Nominal parameters" and "Reduced overhung mass" cases in Fig. 14, respectively. Results show that the high and hot spots of the "Nominal parameters" case continuously change around the journal circumference and instead converge to steady values in the "Reduced overhung mass" case. The phase differences for both cases showed a similar amplitude of approximately 20 deg at the end of the 5-min simulation. The impact of bearing material on the ME instability is investigated here. Bronze has different structural and thermal properties compared with the steel case as listed in Table 3. The bronze material has larger heat conductivity and thermal expansion coefficients than steel. The Young's modulus of the bronze is about

50% of steel, while the density of bronze is about 15% higher than the steel.

Figure 16 shows 1× polar plots at both 8000 rpm and 8800 rpm. Figure 16(*a*) shows that at 8000 rpm the larger spiral vibration occurs with bronze, and it converges more quickly than with steel, during the 5-min simulation period. At 8800 rpm, the vibration amplitude of the bronze shows a much larger amplitude at 5 min compared to the vibration of the steel. The simulation results at two operating speeds show that the FPJB with bronze material generally causes larger ME vibration compared to the FPJB made with the steel material. The critical speed is reduced to 6712 rpm for bronze material as compared to 6929 rpm for steel material. The critical speed change also affects the ME speed range as demonstrated in Ref. [24].

Figure 17 shows bode plots with hysteresis for vibration and journal ΔT for both steel and bronze bearings. The rotor is accelerated from 5000 rpm to 8000 rpm for 2 min and stays at the speed for 2 min. Then, the rotor speed is decreased to 5000 rpm for 1 min. At 8000 rpm, the maximum vibration amplitude at the bearing and journal ΔT is higher with the bronze bearing compared to the steel bearing. The vibration amplitude and ΔT of the bronze decrease more quickly during the run-down compared to steel.

Figure 18 shows the bearing temperature distribution at 5 min and 8800 rpm. Higher temperatures appear with the bronze material in Fig. 18(*a*) compared to the steel bearing in Fig. 18(*b*).

The shaft temperature distributions with the bronze bearing are shown in Figs. 19(*a*) and 19(*b*) at 5 min. In Fig. 19(*a*), the maximum temperature (hot spot) on the shaft circumference is seen to occur at the 99-deg angle. Note that the 0-deg location on the journal circumference is illustrated in Fig. 7(*b*). The highest journal temperature is predicted at the axial center where the

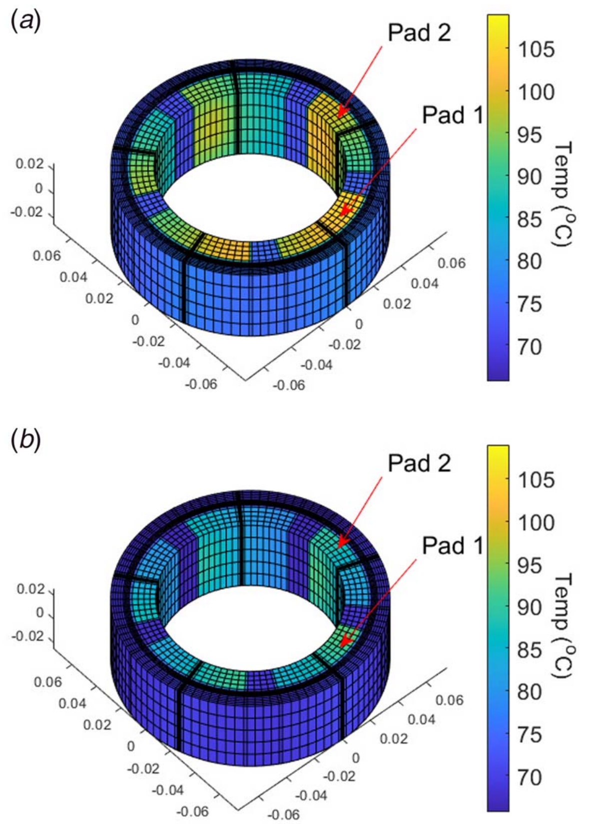

Fig. 18 Simulation results at 5 min (8800 rpm): (*a*) temperature distribution of bronze bearing and (*b*) temperature distribution of steel bearing. Dimensions in meters.

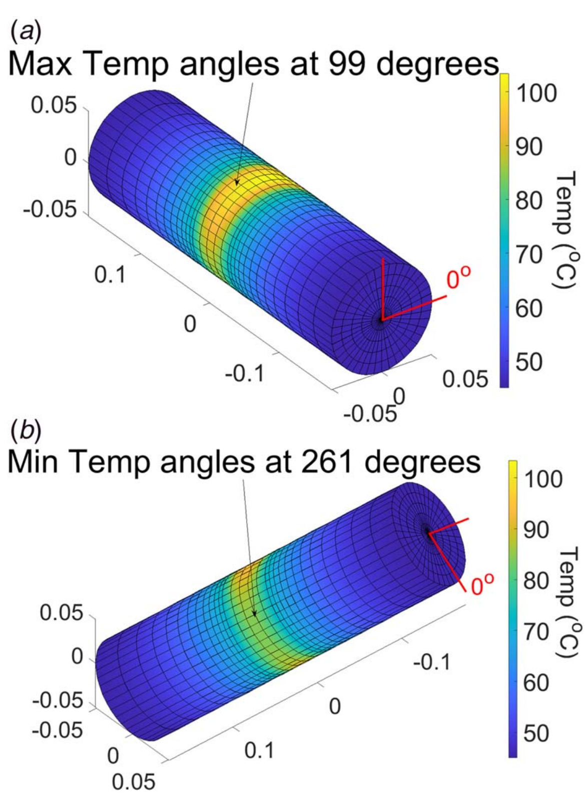

Fig. 19 Simulation results of bronze bearing at 5 min (8800 rpm): (*a*) maximum temperature region of the shaft and (*b*) minimum temperature region of the shaft. Dimensions in meters.

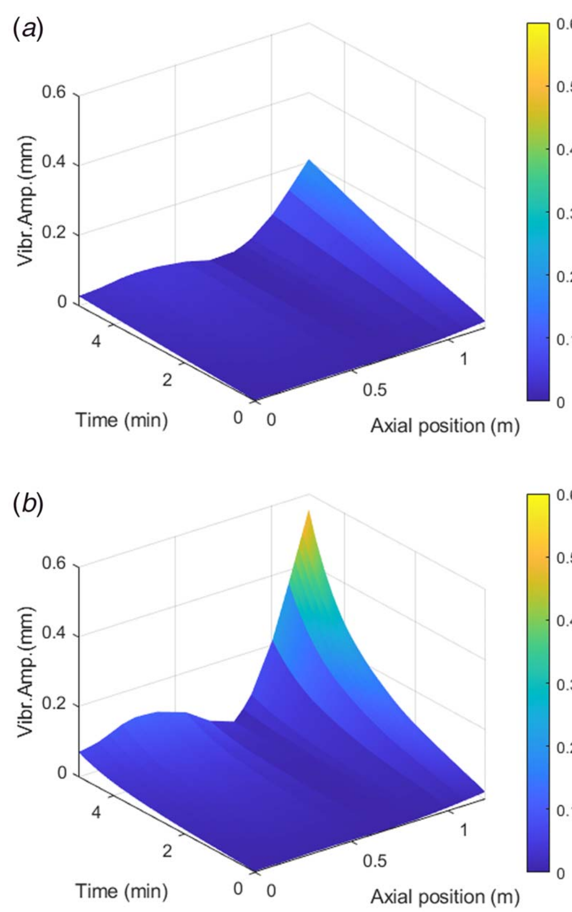

Fig. 20 Vibration distribution along rotor axial direction with time: (*a*) steel and (*b*) bronze at 8800 rpm

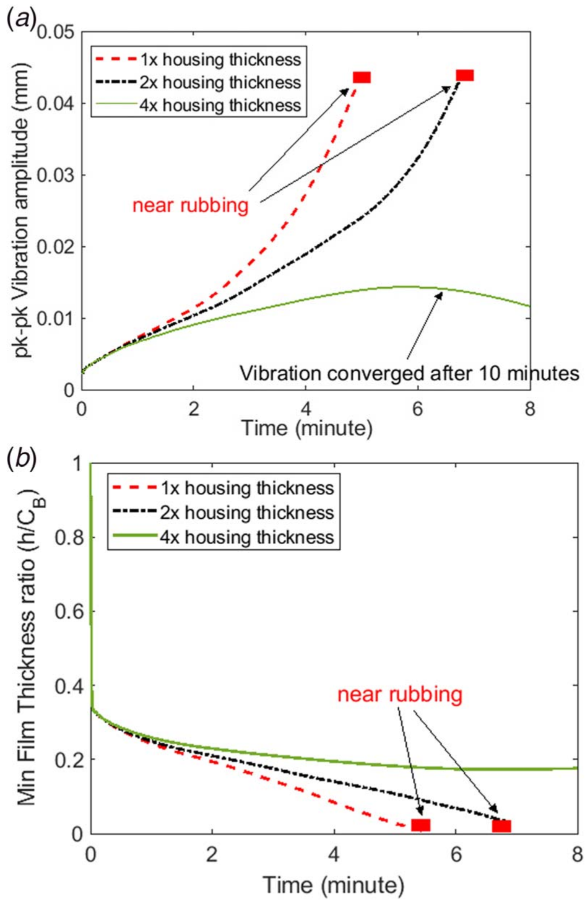

Fig. 21 Effect of bearing housing thickness: (*a*) 1× polar plot and (*b*) minimum film thickness ratio at 8800 rpm

FPJB is located. Meanwhile, the minimum temperature (cold spot) appears near the 261-deg angle, and its value is 82 °C. The difference between these hot and cold spots on the journal circumference induces rotor thermal bow which affects the synchronous vibration.

The vibrations along the rotor axial locations for both steel and bronze materials are shown in Fig. 20. The vibration amplitudes are relatively large at the axial end of the rotor, which indicates that the induced vibration is due to a thermal bow. The vibration level of the bronze case shows maximum pk–pk vibration of 0.6 mm, which is much larger than the amplitude of the steel bearing (around 0.2 mm). These results show that the FPJB bearing with bronze material is more prone to ME instability due to its thermal properties compared with the FPJB made with steel.

The thickness of bearing housing is varied to investigate its impact on the ME vibration. Since the housing is assumed rigid in the structural model, only thermal models are affected by the variation of the housing thicknesses. The geometry of the housing thickness is illustrated in Fig. 3. The nominal thickness of housing was set to 4 mm for the 1× thickness case. As shown in the polar plot in Fig. 21, the amplitude of the spiral vibration at the end of the simulation time is significantly reduced with increasing thicknesses at 8800 rpm. With the thin housing of 1× case, the vibration level reaches up to 0.02 around 4 min and near rubbing occurs at the same instant. The vibration levels are significantly reduced with 2× and 4× cases in Fig. 21(*a*) compared to the 4-mm housing thickness (1×). As shown in Eq. (8), the thermal mass of housing acts as a damping term of the bearing temperature calculations. In this regard, the rate of the thermal inputs into the journal shaft may be affected by the thermal mass of the bearing housing because the bearing-film-shaft thermal structures have coupled with each other. Housing thickness changes affect the thermal expansion of the bearing/housing structures and fluid film temperature. This may influence rotordynamic performance including critical speeds and ME response. The predicted critical speed increased from 6712 rpm with 1× thickness to 6748 rpm for 2× thickness and 6807 rpm for 4× thickness.

5 Conclusions and Future Work

A full 3D thermo-elastohydrodynamic model of flexure pivot bearing is developed, and nonlinear ME simulations have been conducted to verify its modeling. The FPJB-ME model is validated with the experimental results which showed the spiral vibration at 6850 rpm. Extensive parametric studies have been conducted to investigate the design impact of the flexure pivot web. Conclusions include the following:

(1) A simulation was performed for comparison with the experimental Morton effect results in Refs. [36,37]. The developed FPJB-ME model was employed in the simulation, and Morton effect ME was likewise predicted. This required raising the inlet supply temperature by 8 °C and the imbalance magnitude by a factor of 2 in the simulation and yielded a Morton effect onset speed 900 rpm higher than the measured ME onset speed of 6550 rpm. The ME was characterized by high vibration and ΔT. The discrepancy between the ME vibration speed may be explained by the higher critical speed prediction with the current model, which may increase the ME speed range.
(2) The equivalent stiffness-based FPJB model is also introduced, and its accuracy is compared with the full FPJB model. The equivalent model slightly underpredicts the ME vibration and journal ΔT compared to the full model at the same operating speed.
(3) With thicker flexure webs, the ME speed range shifted up to higher operating speeds. By inspecting the critical speed change with different web thicknesses, the first bending critical speed range was found to move up while the damping ratio decreases with thicker webs. Considering most ME cases occurs near the first bending mode of the rotor, the coupling between the critical speed and ME instability speed may attribute the change of ME speed ranges with different web dimensions. In the current study, the thicker web suppressed ME at 8000 rpm and increased ME at 8800 rpm.
(4) Simulations were performed to investigate the effects of web thickness and material, supply oil temperature, bearing radial clearance, and overhung mass on the FPJB-ME. The results showed that there may not exist global solutions to fully suppress the ME since many parameters affect the ME simultaneously. However, the results do show that by developing and employing accurate ME prediction models, the ME instability can be greatly suppressed by selecting optimum parameter sets.
(5) The housing thickness has a significant effect on the ME vibration and journal ΔT levels. With increasing thickness of housing, the suppression effect on ME vibration was observed. Since the thermal mass of the bearing acts as a damping term in the transient thermal models, the increased damping effect with larger thermal mass may reduce the rate of heat input to the journal, thus relatively mitigating the ME vibration compared to the thinner housings. The results show that the thermal mass of bearing housing needs to be considered for accurate ME predictions.

In future work, the flexibility of housing should be considered for an improved prediction model. In Ref. [50], it is shown that the actual pivot stiffness of tilting pad journal bearing is softer than the prediction results, and this may be due to the theoretical model does not account for the housing flexibility. Considering the predicted critical speed of the current model is higher than the experimental result, the inclusion of the housing flexibility may improve the accuracy of the ME predictions. The unmodeled dynamics of the ME model such as the oil inlet mixing physics and 3D solid rotor model need to be considered to improve the accuracy of ME prediction.

Acknowledgment

This research was supported by Texas A&M Turbomachinery Research Consortium.

Conflict of Interest

There are no conflicts of interest.

Data Availability Statement

The data sets generated and supporting the findings of this article are obtainable from the corresponding author upon reasonable request. The authors attest that all data for this study are included in the paper. Data provided by a third party are listed in Acknowledgment. No data, models, or code were generated or used for this paper.

References

[1] Tong, X., Palazzolo, A., and Suh, J., 2017, "A Review of the Rotordynamic Thermally Induced Synchronous Instability (Morton) Effect," ASME Appl. Mech. Rev., **69**(6), p. 060801.
[2] Gu, L., 2018, "A Review of Morton Effect: From Theory to Industrial Practice," Tribol. Trans., **61**(2), pp. 381–391.
[3] de Jongh, F., 2008, "The Synchronous Rotor Instability Phenomenon—Morton Effect," Proceedings of the 37th Turbomachinery Symposium, Houston, TX, Sept. 8–11, pp. 159–167.
[4] Shin, D., Yang, J., Tong, X., Suh, J., and Palazzolo, A., 2020, "A Review of Journal Bearing Thermal Effects on Rotordynamic Response," ASME J. Tribol., **143**(3), p. 031803.
[5] Kim, S., Shin, D., and Palazzolo, A. B., 2021, "A Review of Journal Bearing Induced Nonlinear Rotordynamic Vibrations," ASME J. Tribol., **143**(11), p. 111802.
[6] Morton, P. G., 1975, "Some Aspects of Thermal Instability in Generators," G.E.C. Internal Report No. S/W40 u183.
[7] de Jongh, F. M., and Morton, P. G., 1996, "The Synchronous Instability of a Compressor Rotor Due to Bearing Journal Differential Heating," ASME J. Eng. Gas Turbines Power, **118**(4), pp. 816–824.
[8] de Jongh, F., and Van Der Hoeven, P.1998, "Application of a Heat Barrier Sleeve to Prevent Synchronous Rotor Instability," Proceedings of the 27th Turbomachinery Symposium, Houston, TX, Sept. 20–24, pp. 17–26.
[9] Berot, F., and Dourlens, H., 1999, "On Instability of Overhung Centrifugal Compressors," ASME Paper No. 99-GT-202.
[10] Keogh, P. S., and Morton, P. G., 1993, "Journal Bearing Differential Heating Evaluation With Influence on Rotor Dynamic Behaviour," Proc. R. Soc. London Ser. A, **441**(1913), pp. 527–548.
[11] Keogh, P., and Morton, P., 1994, "The Dynamic Nature of Rotor Thermal Bending Due to Unsteady Lubricant Shearing Within a Bearing," Proc. R. Soc. London Ser. A, **445**(1924), pp. 273–290.
[12] Tucker, P. G., and Keogh, P. S., 1996, "On the Dynamic Thermal State in a Hydrodynamic Bearing With a Whirling Journal Using CFD Techniques," ASME J. Tribol., **118**(2), pp. 356–363.
[13] Gomiciaga, R., and Keogh, P. S., 1999, "Orbit Induced Journal Temperature Variation in Hydrodynamic Bearings," ASME J. Tribol., **121**(1), pp. 77–84.
[14] Kellenberger, W., 1980, "Spiral Vibrations Due to the Seal Rings in Turbogenerators Thermally Induced Interaction Between Rotor and Stator," ASME J. Mech. Des., **102**(1), pp. 177–184.
[15] Kirk, G., Guo, Z., and Balbahadur, A., 2003, "Synchronous Thermal Instability Prediction for Overhung Rotors," Proceedings of the 32nd Turbomachinery Symposium, Houston, TX, Sept. 8–11, pp. 121–135.
[16] Eckert, L., and Schmied, J., 2008, "Spiral Vibration of a Turbogenerator Set: Case History, Stability Analysis, Measurements and Operational Experience," ASME J. Eng. Gas Turbines Power, **130**(1), p. 012509.
[17] Murphy, B. T., and Lorenz, J. A., 2010, "Simplified Morton Effect Analysis for Synchronous Spiral Instability," ASME J. Vib. Acoust., **132**(5), p. 051008.
[18] Childs, D. W., and Saha, R., 2012, "A New, Iterative, Synchronous-Response Algorithm for Analyzing the Morton Effect," ASME J. Eng. Gas Turbines Power, **134**(7), p. 072501.
[19] Lee, J. G., and Palazzolo, A., 2012, "Morton Effect Cyclic Vibration Amplitude Determination for Tilt Pad Bearing Supported Machinery," ASME J. Tribol., **135**(1), p. 011701.
[20] Suh, J., and Palazzolo, A., 2014, "Three-Dimensional Thermohydrodynamic Morton Effect Simulation—Part I: Theoretical Model," ASME J. Tribol., **136**(3), p. 031706.
[21] Suh, J., and Palazzolo, A., 2014, "Three-Dimensional Thermohydrodynamic Morton Effect Analysis—Part II: Parametric Studies," ASME J. Tribol., **136**(3), p. 031707.
[22] Tong, X., Palazzolo, A., and Suh, J., 2016, "Rotordynamic Morton Effect Simulation With Transient, Thermal Shaft Bow," ASME J. Tribol., **138**(3), p. 031705.
[23] Tong, X., and Palazzolo, A., 2016, "Double Overhung Disk and Parameter Effect on Rotordynamic Synchronous Instability—Morton Effect—Part I: Theory and Modeling Approach," ASME J. Tribol., **139**(1), p. 011705.
[24] Tong, X., and Palazzolo, A., 2016, "Double Overhung Disk and Parameter Effect on Rotordynamic Synchronous Instability—Morton Effect—Part II: Occurrence and Prevention," ASME J. Tribol., **139**(1), p. 011706.
[25] Tong, X., and Palazzolo, A., 2018, "Tilting Pad Gas Bearing Induced Thermal Bow Rotor Instability," Tribol. Int., **121**, pp. 269–279.
[26] Panara, D., Panconi, S., and Griffini, D., 2015, "Numerical Prediction and Experimental Validation of Rotor Thermal Instability," Proceedings of the 44th Turbomachinery Symposium, Houston, TX, Sept. 14–17, pp. 1–18.
[27] Shin, D., and Palazzolo, A. B., 2020, "Tilting Pad Journal Bearing Misalignment Effect on Thermally Induced Synchronous Instability (Morton Effect)," ASME J. Tribol., **143**(3), p. 031802.
[28] Shin, D., and Palazzolo, A. B., 2021, "Tilting Pad Bearing Pivot Friction and Design Effects on Thermal Bow-Induced Rotor Vibration," ASME J. Tribol., **143**(12), p. 121804.
[29] Shin, D., Palazzolo, A. B., and Tong, X., 2020, "Squeeze Film Damper Suppression of Thermal Bow-Morton Effect Instability," ASME J. Eng. Gas Turbines Power, **142**(12), p. 121013.
[30] Guo, Z., and Kirk, G., 2011, "Morton Effect Induced Synchronous Instability in Mid-Span Rotor–Bearing Systems—Part I: Mechanism Study," ASME J. Vib. Acoust., **133**(6), p. 061004.
[31] Guo, Z., and Kirk, G., 2011, "Morton Effect Induced Synchronous Instability in Mid-Span Rotor–Bearing Systems, Part 2: Models and Simulations," ASME J. Vib. Acoust., **133**(6), p. 061006.
[32] Lorenz, J., and Murphy, B., 2011, "Case Study of Morton Effect Shaft Differential Heating in a Variable-Speed Rotating Electric Machine," ASME Paper NO. GT2011-45228.
[33] Tong, X., and Palazzolo, A., 2017, "Measurement and Prediction of the Journal Circumferential Temperature Distribution for the Rotordynamic Morton Effect," ASME J. Tribol., **140**(3), p. 031702.
[34] Hresko, A., Shin, D., and Palazzolo, A. B., 2019, "Experimental Investigation of Morton Effect (Thermally Induced Rotor Instability)," ASME Paper No. GT2019-92281.
[35] Plantegenet, T., Arghir, M., Hassini, M. A., and Jolly, P., 2020, "The Thermal Unbalance Effect Induced by a Journal Bearing in Rigid and Flexible Rotors: Experimental Analysis," Tribol. Trans., **63**(1), pp. 52–67.
[36] Plantegenet, T., Arghir, M., and Jolly, P., 2020, "Experimental Analysis of the Thermal Unbalance Effect of a Flexible Rotor Supported by a Flexure Pivot Tilting Pad Bearing," Mech. Syst. Signal Process., **145**, p. 106.
[37] Plantegenet, T., 2019, "Analyse Expérimentale de L'effet Morton," PhD dissertation, Université de Poitiers, Poitiers.
[38] Walton, N. V., and San Andres, L., 1997, "Measurements of Static Loading Versus Eccentricity in a Flexure-Pivot Tilting Pad Journal Bearing," ASME J. Tribol., **119**(2), pp. 297–304.
[39] Rodriguez, L. E., and Childs, D. W., 2005, "Frequency Dependency of Measured and Predicted Rotordynamic Coefficients for a Load-On-Pad Flexible-Pivot Tilting-Pad Bearing," ASME J. Tribol., **128**(2), pp. 388–395.
[40] Al-Ghasem, A. M., and Childs, D. W., 2005, "Rotordynamic Coefficients Measurements Versus Predictions for a High-Speed Flexure-Pivot Tilting-Pad Bearing (Load-Between-Pad Configuration)," ASME J. Eng. Gas Turbines Power, **128**(4), pp. 896–906.
[41] Hensley, J. E., and Childs, D., 2008, "Measurements Versus Predictions for Rotordynamic Characteristics of a Flexure Pivot-Pad Tilting Pad Bearing in an LBP Condition at Higher Unit Loads," ASME Paper No. GT2008-50066.
[42] Vannini, G., Cangioli, F., Ciulli, E., Nuti, M., Forte, P., Kim, J., and Livermore-Hardy, R., 2020, "Experiments on a Large Flexure Pivot Journal Bearing: Summary of Test Results and Comparison With Predictions," ASME J. Eng. Gas Turbines Power, **142**(3), p. 031004.
[43] Armentrout, R. W., and Paquette, D. J., 1993, "Rotordynamic Characteristics of Flexure-Pivot Tilting-Pad Journal Bearings," Tribol. Trans., **36**(3), pp. 443–451.
[44] Chen, W. J., 1995, "Bearing Dynamic Coefficients of Flexible-Pad Journal Bearings," Tribol. Trans., **38**(2), pp. 253–260.
[45] San Andres, L., 1996, "Turbulent Flow, Flexure-Pivot Hybrid Bearings for Cryogenic Applications," ASME J. Tribol., **118**(1), pp. 190–200.
[46] Kim, T. H., Jang, K. E., and Choi, T. G., 2016, "Rotordynamics Performance Predictions of Flexure Pivot Tilting Pad Bearings and Comparison to Published Test Data," ASME Paper No. GT2016-56284.
[47] Suh, J., Palazzolo, A., and Choi, Y., 2017, "Numerical Modeling and Analysis of Flexure-Pivot Tilting-Pad Bearing," ASME J. Tribol., **139**(5), p. 051704.
[48] Sim, K., and Kim, D., 2006, "Design of Flexure Pivot Tilting Pads Gas Bearings for High-Speed Oil-Free Microturbomachinery," ASME J. Tribol., **129**(1), pp. 112–119.
[49] Sim, K., and Kim, D., 2008, "Thermohydrodynamic Analysis of Compliant Flexure Pivot Tilting Pad Gas Bearings," ASME J. Eng. Gas Turbines Power, **130**(3), p. 032502.
[50] Dang, P. V., Chatterton, S., and Pennacchi, P., 2019, "The Effect of the Pivot Stiffness on the Performances of Five-Pad Tilting Pad Bearings," Lubricants, **7**(7), p. 61.